PERGAMON

Computers and Structures 77 (2000) 453–460

Computers & Structures

www.elsevier.com/locate/compstruc

Dynamic instability of composite laminates using a higher order theory

Aditi Chattopadhyay *, Adrian G. Radu

Department of Mechanical and Aerospace Engineering, Arizona State University, Tempe, AZ 85287-6106, USA

Received 13 November 1998; accepted 14 December 1999

Abstract

A higher order shear deformation theory is used to investigate the instability associated with composite plates subject to dynamic loads. Both transverse shear and rotary inertia effects are taken into account. The procedure is implemented using the finite element approach. The natural frequencies and the critical buckling load are computed and compared with the results based on the classical laminate plate theory and the first-order shear deformation theory. The first two instability regions are determined for various loading conditions using both first- and second-order approximations. These results are also compared with the other approaches. Significant deviations are observed for thick plates due to the presence of shear deformation.

Keywords: Dynamic stability; Higher order theory; Composite plates; Buckling

1. Introduction

Composites are increasingly being used in the design of load-carrying members for the aerospace applications. As a result, much research has been devoted to study the static and dynamic responses of composites under different loading conditions. In studying the behavior of these structures under static and dynamic buckling loads, the classical and the first-order plate theories, have been shown to underpredict the deflections and to overpredict the buckling loads and the natural frequencies [1–3]. The higher order theories (HOT), which more accurately model the transverse shear effects, have been shown to predict better results [4–6].

A variationally consistent higher order theory [7] is used to investigate the dynamic buckling of composite plates in the current study. This theory assumes a cubic distribution for the in-plane displacements through the thickness and satisfies the stress free boundary conditions at the top and bottom surfaces of the laminate. Composite plates with various geometry and boundary conditions are analyzed. The bending natural frequencies and the critical buckling loads are computed and compared with those obtained with the classical laminate plate theory (CLPT) and the first-order shear deformation theory (FSDT). The first- and second-order approximations of the first two instability regions are determined and compared with those obtained using the CLPT and FSDT.

2. Problem formulation

A composite plate with the coordinate plane (x, y) as the middle plane and the z axis along the thickness direction is considered. The in-plane displacements u and v of an arbitrary point within the plate is assumed [7,8] as a cubic polynomial in z, whereas the out-of-plane displacement w is considered to be independent with respect to the thickness as follows:

* Corresponding author. Tel.: +1-480-965-9342; fax: +1-480-965-1384.

E-mail address: aditi@asu.edu (A. Chattopadhyay).

0045-7949/00/$ - see front matter
PII: S0045-7949(00)00005-5

$$
\begin{aligned}
u &= u_0 + z\left(\alpha - \frac{\partial w}{\partial x}\right) + z^2\chi + z^3\xi,\\
v &= v_0 + z\left(\beta - \frac{\partial w}{\partial y}\right) + z^2\eta + z^3\zeta,\\
w &= w_0,
\end{aligned}
\tag{1}
$$

where the mid-plane displacements u_0, v_0 and w_0 and the polynomial coefficients α, β, χ, η, ξ, and ζ are time-dependent functions of the in-plane coordinates x and y. It must be noted that if the quadratic and cubic terms are ignored in Eq. (1), the displacement field is equivalent to the one which characterizes the FSDT. If α and β are also set to zero, the CLPT displacement field is obtained.

The von Karman strain displacement relations are used for modeling the moderate displacements and the small rotations that characterize the deformed buckled state:

$$
\begin{aligned}
\varepsilon_x &= \frac{\partial u}{\partial x} + \frac{1}{2}\left(\frac{\partial w}{\partial x}\right)^2, \quad \varepsilon_y = \frac{\partial v}{\partial y} + \frac{1}{2}\left(\frac{\partial w}{\partial y}\right)^2,\\
\gamma_{xy} &= \frac{\partial u}{\partial y} + \frac{\partial v}{\partial x} + \frac{\partial w}{\partial x}\frac{\partial w}{\partial y},\\
\varepsilon_z &= \frac{\partial w}{\partial z}, \quad \gamma_{yz} = \frac{\partial v}{\partial z} + \frac{\partial w}{\partial y},\\
\gamma_{zx} &= \frac{\partial u}{\partial z} + \frac{\partial w}{\partial x}.
\end{aligned}
\tag{2}
$$

The displacement field must satisfy the stress free boundary conditions on the top and bottom surfaces of the laminate. That is

$$
\left[\tau_{yz}\right]_{z=\pm h/2} = 0 \quad \text{and} \quad \left[\tau_{zx}\right]_{z=\pm h/2} = 0, \tag{3}
$$

where h is the laminate thickness. For an orthotropic laminate, this is equivalent to

$$
\left[\varepsilon_{yz}\right]_{z=\pm h/2} = 0 \quad \text{and} \quad \left[\varepsilon_{zx}\right]_{z=\pm h/2} = 0. \tag{4}
$$

By substituting Eq. (1) into the strain–displacement relations (2) and by imposing the boundary conditions (4) on the obtained results, some of the higher order terms in Eq. (1) can be identified in terms of the lower order terms. The final form of the displacement field can now be written as follows:

$$
\begin{aligned}
u &= u_0 + z\left(\alpha - \frac{\partial w}{\partial x}\right) - \frac{4\alpha}{3h^2}z^3,\\
v &= v_0 + z\left(\beta - \frac{\partial w}{\partial y}\right) - \frac{4\beta}{3h^2}z^3,\\
w &= w_0,
\end{aligned}
\tag{5}
$$

where α and β are the rotations of the transverse normal with respect to the x and y axes, respectively. The total strain, ε, can be expressed in matrix form as follows:

$$
\begin{aligned}
\varepsilon &= \begin{Bmatrix} \varepsilon_{\mathrm{LN}} \\ \mathbf{0} \end{Bmatrix} + z\begin{Bmatrix} \varepsilon_1 \\ \mathbf{0} \end{Bmatrix} + z^3\begin{Bmatrix} \varepsilon_3 \\ \mathbf{0} \end{Bmatrix} + \begin{Bmatrix} \mathbf{0} \\ \varepsilon_{\mathrm{s}} \end{Bmatrix} + z^2\begin{Bmatrix} \mathbf{0} \\ \varepsilon_{\mathrm{s2}} \end{Bmatrix},\\
\varepsilon_{\mathrm{LN}} &= \varepsilon_0 + \varepsilon_{\mathrm{N}}.
\end{aligned}
\tag{6}
$$

In Eq. (6), ε_0 and ε_{N} are the mid-plane and the nonlinear strains. The quantities ε_1 and ε_3 are the bending strains corresponding to the linear and the cubic variation in z, ε_{s} is the mid-plane shear strain and $\varepsilon_{\mathrm{s2}}$ is the shear strain corresponding to the quadratic variation in z. They are expressed as follows:

$$
\begin{aligned}
\varepsilon_0 &= \begin{Bmatrix} \frac{\partial u_0}{\partial x} \\ \frac{\partial v_0}{\partial y} \\ \frac{\partial v_0}{\partial x} + \frac{\partial u_0}{\partial y} \end{Bmatrix}, \quad \varepsilon_{\mathrm{N}} = \frac{1}{2}\begin{Bmatrix} \left(\frac{\partial w_0}{\partial x}\right)^2 \\ \left(\frac{\partial w_0}{\partial y}\right)^2 \\ 2\frac{\partial w_0}{\partial x}\frac{\partial w_0}{\partial y} \end{Bmatrix},\\
\varepsilon_1 &= \begin{Bmatrix} \frac{\partial \alpha}{\partial x} - \frac{\partial^2 w_0}{\partial x^2} \\ \frac{\partial \beta}{\partial y} - \frac{\partial^2 w_0}{\partial y^2} \\ \frac{\partial \alpha}{\partial y} + \frac{\partial \beta}{\partial x} - 2\frac{\partial^2 w_0}{\partial x \partial y} \end{Bmatrix},\\
\varepsilon_3 &= k\begin{Bmatrix} \frac{\partial \alpha}{\partial x} \\ \frac{\partial \beta}{\partial y} \\ \frac{\partial \alpha}{\partial y} + \frac{\partial \beta}{\partial x} \end{Bmatrix}, \quad \varepsilon_{\mathrm{s}} = \begin{Bmatrix} \beta \\ \alpha \end{Bmatrix}, \quad \varepsilon_{\mathrm{s2}} = \frac{k}{3}\begin{Bmatrix} \beta \\ \alpha \end{Bmatrix}\\
&\text{where } k = -\frac{4}{h^2}
\end{aligned}
\tag{7}
$$

The stress resultant vector is defined as $\hat{\sigma}^{\mathrm{T}} = \left\{\mathbf{N}^{\mathrm{T}}\mathbf{M}^{\mathrm{T}}\mathbf{P}^{\mathrm{T}}\mathbf{Q}^{\mathrm{T}}\mathbf{R}^{\mathrm{T}}\right.$, where $\mathbf{N}$, $\mathbf{M}$ and $\mathbf{Q}$ are the in-plane force resultant vectors and $\mathbf{P}$ and $\mathbf{R}$ denote the higher order stress resultant vectors. The constitutive relation can be written as $\hat{\sigma} = \mathbf{C}\varepsilon$, where the strain vector is $\varepsilon^{\mathrm{T}} = \{\varepsilon_{\mathrm{LN}}^{\mathrm{T}}\varepsilon_1^{\mathrm{T}}\varepsilon_3^{\mathrm{T}}\varepsilon_{\mathrm{s}}^{\mathrm{T}}\varepsilon_{\mathrm{s2}}^{\mathrm{T}}\}$ and $\mathbf{C}$, the stiffness matrix.

The equation of motion is derived using Hamilton's principle

$$
\delta\prod = \int_{t_1}^{t_2}(\delta T - \delta U + \delta W)\,\mathrm{d}t = 0, \tag{8}
$$

where T, U and W are the kinetic energy, the strain energy and the work done by the external loads respectively. Using Eq. (7), the strain energy variation (8) is expanded in the following form:

$$
\begin{aligned}
\delta U = \int_{\Omega} &\left[\delta\varepsilon_{\mathrm{LN}}^{\mathrm{T}}\mathbf{A}\varepsilon_{\mathrm{LN}} + \delta\varepsilon_{\mathrm{LN}}^{\mathrm{T}}\mathbf{B}\varepsilon_1 + \delta\varepsilon_{\mathrm{LN}}^{\mathrm{T}}\mathbf{E}\varepsilon_3\right.\\
&\left. + \delta\varepsilon_1^{\mathrm{T}}\mathbf{B}\varepsilon_{\mathrm{LN}} + \delta\varepsilon_1^{\mathrm{T}}\mathbf{D}\varepsilon_1 + \delta\varepsilon_1^{\mathrm{T}}\mathbf{F}\varepsilon_3\right]\mathrm{d}\Omega\\
+ \int_{\Omega} &\left[\delta\varepsilon_3^{\mathrm{T}}\mathbf{E}\varepsilon_{\mathrm{LN}} + \delta\varepsilon_3^{\mathrm{T}}\mathbf{F}\varepsilon_1 + \delta\varepsilon_3^{\mathrm{T}}\mathbf{H}\varepsilon_3 + \delta\varepsilon_{\mathrm{s}}^{\mathrm{T}}\mathbf{A}_{\mathrm{s}}\varepsilon_{\mathrm{s}}\right.\\
&\left. + \delta\varepsilon_{\mathrm{s}}^{\mathrm{T}}\mathbf{D}_{\mathrm{s}}\varepsilon_{\mathrm{s2}} + \delta\varepsilon_{\mathrm{s2}}^{\mathrm{T}}\mathbf{D}_{\mathrm{s}}\varepsilon_{\mathrm{s}} + \delta\varepsilon_{\mathrm{s2}}^{\mathrm{T}}\mathbf{F}_{\mathrm{s}}\varepsilon_{\mathrm{s2}}\right]\mathrm{d}\Omega.
\end{aligned}
\tag{9}
$$

In Eq. (9), the components $\mathbf{A}$ and $\mathbf{A}_{\mathrm{s}}$ are the extensional stiffness matrices, $\mathbf{B}$ and $\mathbf{B}_{\mathrm{s}}$ are the bending-extensional coupling matrices, $\mathbf{D}$ and $\mathbf{D}_{\mathrm{s}}$ are the bending

stiffness matrices and **E**, **F**, $\mathbf{F}_s$ and **H** are higher order stiffness matrices [8]. Subscript 's' denotes the shear effects.

After integration by parts with respect to time, the kinetic energy variation is expressed in terms of the displacement vector $\{\mathbf{d}\}^T = \{u, v, w\}$ and its second derivative with respect to time as follows:

$$\delta T = -\int_\Omega \rho\{\delta\mathbf{d}^T\}\{\ddot{\mathbf{d}}\}\,d\Omega. \tag{10}$$

The variation of the work done by the buckling force F_x is written [9] as follows:

$$\delta W = \frac{1}{2}\int_\Omega F_x\left(\frac{\partial w}{\partial x}\right)^2 d\Omega. \tag{11}$$

3. Finite element formulation

For deriving the governing equation of the plate, the strains in Eq. (9), the second-order time derivative in Eq. (10) and the partial derivative of the transverse displacement from Eq. (11) are expressed in terms of the vector of the unknown functions $\mathbf{u} = \{u, \alpha, v, \beta, w\}^T$ following the procedure described in Refs. [10,11]. The vector **u** is then expressed in terms of the nodal unknowns $\mathbf{q} = \{u, \alpha, v, \beta, w, \partial w/\partial x, \partial w/\partial y, \partial^2 w/(\partial x \partial y)\}^T$ using the bilinear interpolation for u, α, v and β and 16-term cubic interpolation for w. The finite element analysis is performed using a quadrilateral element with four nodes and eight degrees of freedom per node. The governing equation of the plate is obtained in matrix form as follows:

$$\mathbf{M}\ddot{\mathbf{q}} + [\mathbf{K}_L + \mathbf{K}_{NL} + \mathbf{K}_{NN}]\mathbf{q} + F_x\mathbf{K}_G\mathbf{q} = 0, \tag{12}$$

where **M** is the mass matrix, $\mathbf{K}_L$, the linear stiffness matrix, $\mathbf{K}_{NL}$ and $\mathbf{K}_{NN}$ are the nonlinear stiffness matrices and $\mathbf{K}_G$ is the geometric stiffness matrix. These stiffness matrices are obtained by grouping the terms in Eq. (9). In the present study, only the linear buckling analysis is performed; therefore, the nonlinear stiffness matrices in Eq. (12) are not considered. The geometric stiffness matrix, $\mathbf{K}_G$, is computed by assembling for the entire plate, elemental matrix [11]:

$$\mathbf{K}_G^e = \int_{\Omega_e} \mathbf{G}_e^T\mathbf{T}\mathbf{G}_e\,d\Omega_e,$$

where

$$\mathbf{G}_e = \sum_{j=1}^{4}[\mathbf{0} \quad d\mathbf{H}_j] \quad \text{and} \quad \mathbf{T} = \begin{bmatrix} N_x & N_{xy} \\ N_{xy} & N_y \end{bmatrix}. \tag{13}$$

The geometric stiffness matrix $\mathbf{G}_e$ in Eq. (13) is expressed using the matrix of derivatives $d\mathbf{H}_j$ of the cubic shape functions with respect to x and y coordinates, and the summation symbol indicates horizontal augmentation of the four nodal matrices. The **T** matrix in Eq. (13) is the load matrix in which, for unidirectional buckling, only the first component on the main diagonal is nonzero.

4. Stability analysis

The stability analysis of the plate is performed by expressing the dynamic buckling load F_x in terms of the critical buckling load (P_{cr}) as follows:

$$F_x = \alpha_0 P_{cr} + \alpha_1 P_{cr}\cos(\theta t), \tag{14}$$

where α_0 and α_1 are the static and dynamic parameters taking values from 0 to 1. After substituting the buckling load (14) into Eq. (12), the governing equation of the plate is written as follows:

$$\mathbf{M}\ddot{\mathbf{q}} + [\mathbf{K}_L + \alpha_0 P_{cr}\mathbf{K}_G]\mathbf{q} + (\alpha_1 P_{cr}\cos(\theta t))\mathbf{K}_G\mathbf{q} = \mathbf{0}. \tag{15}$$

Eq. (15) is a Mathieu type equation, describing the nonlinear instability behavior of the plate subjected to an in-plane load which has a static and a dynamic component. The generalized eigenvalue problem obtained from Eq. (15) is solved by neglecting both the terms containing P_{cr} to obtain the natural frequencies. If the harmonic and the mass terms are neglected, the new generalized eigenvalue problem yields the critical buckling load. If only the harmonic term is neglected, Eq. (15) yields the natural frequency of the loaded plate, the load being $\alpha_0 P_{cr}$, a static compressive force. The instability regions are determined [12] from the boundaries of instability, which represent the periodic solutions of Eq. (15). These solutions are

$$\begin{aligned} \mathbf{q} &= \frac{1}{2}\mathbf{b}_0 + \sum_{i=2,4,\ldots}^{\infty}(\mathbf{a}_i\sin(i\theta t/2) + \mathbf{b}_i\cos(i\theta t/2)), \\ \mathbf{q} &= \sum_{i=1,3,\ldots}^{\infty}(\mathbf{a}_i\sin(i\theta t/2) + \mathbf{b}_i\cos(i\theta t/2)). \end{aligned} \tag{16}$$

Substituting solutions (16) into Eq. (15) and by grouping the sine and cosine terms, two sets of linear algebraic equations in $\mathbf{a}_i$ and $\mathbf{b}_i$ are obtained for each solution. To obtain the nontrivial coefficient vectors $\mathbf{a}_i$ and $\mathbf{b}_i$, the determinant of the coefficient matrix has to be zero for each of the four sets. These determinants are infinite as the series in solution (16) is infinite and belong to a class of converging determinants called the normal determinants [12].

The first term solutions derived from Eq. (16) are

$$\begin{aligned} \mathbf{q} &= \tfrac{1}{2}\mathbf{b}_0 + \mathbf{a}_2\sin(\theta t) + \mathbf{b}_2\cos(\theta t), \\ \mathbf{q} &= \mathbf{a}_1\sin(\theta t/2) + \mathbf{b}_1\cos(\theta t/2). \end{aligned} \tag{17}$$

For nontrivial solutions, the resulting determinants must be zero. This leads to the following generalized eigenvalue problems:

$$\mathbf{K}+(\alpha_0-0.5\alpha_1)\lambda_{cr}\mathbf{K}_G\pm\mathbf{M}\frac{\theta_1^2}{4}=\mathbf{0}, \tag{18a}$$

$$\mathbf{K}+\alpha_0\lambda_{cr}\mathbf{K}_G-\mathbf{M}\theta_1^2=\mathbf{0}, \tag{18b}$$

$$\begin{bmatrix}\mathbf{K}+\alpha_0\lambda_{cr}\mathbf{K}_G & 0.5\alpha_1\lambda_{cr}\mathbf{K}_G\\ \alpha_1\lambda_{cr}\mathbf{K}_G & \mathbf{K}+\alpha_0\lambda_{cr}\mathbf{K}_G\end{bmatrix}-\begin{bmatrix}\mathbf{0} & \mathbf{0}\\ \mathbf{0} & \mathbf{M}\end{bmatrix}\theta_1^2=0. \tag{18c}$$

The solutions of Eqs. (18a)–(18c) determine the first-order approximation of the instability regions. Eq. (18a) determines the two boundaries of the first region of dynamic instability, whereas Eqs. (18b) and (18c) determine the upper and lower boundaries of the second instability region. In Eqs. (18a)–(18c), θ_1 represents the first-order approximation of the parametric resonance frequency.

The two term solutions obtained from Eq. (16) are

$$\begin{aligned}\mathbf{q}&=\tfrac{1}{2}\mathbf{b}_0+\mathbf{a}_2\sin(\theta t)+\mathbf{b}_2\cos(\theta t)+\mathbf{a}_4\sin(2\theta t)\\&\quad+\mathbf{b}_4\cos(2\theta t)\\ \mathbf{q}&=\mathbf{a}_1\sin(\theta t/2)+\mathbf{b}_1\cos(\theta t/2)+\mathbf{a}_3\sin(3\theta t/2)\\&\quad+\mathbf{b}_3\cos(3\theta t/2).\end{aligned} \tag{19}$$

Following the same procedure, the generalized eigenvalue problems are obtained. When solved directly, they determine the third and fourth instability regions besides the first two instability regions, which are also obtained from Eqs. (18a)–(18c).

$$\begin{bmatrix}\mathbf{K}+(\alpha_0\pm0.5\alpha_1)\lambda_{cr}\mathbf{K}_G & 0.5\alpha_1\mathbf{K}_G\\ 0.5\alpha_1\mathbf{K}_G & \mathbf{K}+\alpha_0\lambda_{cr}\mathbf{K}_G\end{bmatrix}-\begin{bmatrix}\frac{1}{4}\mathbf{M} & \mathbf{0}\\ \mathbf{0} & \frac{9}{4}\mathbf{M}\end{bmatrix}\theta^2=\mathbf{0}, \tag{20a}$$

$$\begin{bmatrix}\mathbf{K}+(\alpha_0\pm0.5\alpha_1)\lambda_{cr}\mathbf{K}_G & 0.5\alpha_1\lambda_{cr}\mathbf{K}_G & \mathbf{0}\\ 0.5\alpha_1\lambda_{cr}\mathbf{K}_G & \mathbf{K}+\alpha_0\lambda_{cr}\mathbf{K}_G & 0.5\alpha_1\lambda_{cr}\mathbf{K}_G\\ \mathbf{0} & 0.5\alpha_1\lambda_{cr}\mathbf{K}_G & \mathbf{K}+\alpha_0\lambda_{cr}\mathbf{K}_G\end{bmatrix}-\begin{bmatrix}\mathbf{M} & \mathbf{0} & \mathbf{0}\\ \mathbf{0} & 4\mathbf{M} & \mathbf{0}\\ \mathbf{0} & \mathbf{0} & 8\mathbf{M}\end{bmatrix}\theta^2=\mathbf{0}, \tag{20b}$$

$$\begin{bmatrix}\mathbf{K}+(\alpha_0\pm0.5\alpha_1)\lambda_{cr}\mathbf{K}_G & 0.5\alpha_1\lambda_{cr}\mathbf{K}_G & \mathbf{0} & \mathbf{0}\\ \alpha_1\lambda_{cr}\mathbf{K}_G & \mathbf{K}+\alpha_0\lambda_{cr}\mathbf{K}_G & 0.5\alpha_1\lambda_{cr}\mathbf{K}_G & \mathbf{0}\\ \mathbf{0} & 0.5\alpha_1\lambda_{cr}\mathbf{K}_G & \mathbf{K}+\alpha_0\lambda_{cr}\mathbf{K}_G & 0.5\alpha_1\lambda_{cr}\mathbf{K}_G\\ \mathbf{0} & \mathbf{0} & 0.5\alpha_1\lambda_{cr}\mathbf{K}_G & \mathbf{K}+\alpha_0\lambda_{cr}\mathbf{K}_G\end{bmatrix}-\begin{bmatrix}\mathbf{0} & \mathbf{0} & \mathbf{0} & \mathbf{0}\\ \mathbf{0} & \mathbf{M} & \mathbf{0} & \mathbf{0}\\ \mathbf{0} & \mathbf{0} & 4\mathbf{M} & \mathbf{0}\\ \mathbf{0} & \mathbf{0} & \mathbf{0} & 8\mathbf{M}\end{bmatrix}\theta^2=\mathbf{0}. \tag{20c}$$

By solving Eqs. (20a)–(20c), in an iterative manner, the corrected first two instability regions are obtained from the new eigenvalue problems. For example, Eqs. (20a) and (20b) are presented in their iterative form in Eq. (21)

$$\begin{bmatrix}\mathbf{K}+(\alpha_0\pm0.5\alpha_1)\lambda_{cr}\mathbf{K}_G & 0.5\alpha_1\mathbf{K}_G\\ 0.5\alpha_1\mathbf{K}_G & \mathbf{K}+\alpha_0\lambda_{cr}\mathbf{K}_G-\frac{9}{4}\mathbf{M}\theta_1^2\end{bmatrix}-\begin{bmatrix}\frac{1}{4}\mathbf{M} & \mathbf{0}\\ \mathbf{0} & \mathbf{0}\end{bmatrix}\theta_2^2=\mathbf{0},$$
$$\begin{bmatrix}\mathbf{K}+(\alpha_0\pm0.5\alpha_1)\lambda_{cr}\mathbf{K}_G & 0.5\alpha_1\lambda_{cr}\mathbf{K}_G & \mathbf{0}\\ 0.5\alpha_1\lambda_{cr}\mathbf{K}_G & \mathbf{K}+\alpha_0\lambda_{cr}\mathbf{K}_G-4\mathbf{M}\theta_1^2 & 0.5\alpha_1\lambda_{cr}\mathbf{K}_G\\ \mathbf{0} & 0.5\alpha_1\lambda_{cr}\mathbf{K}_G & \mathbf{K}+\alpha_0\lambda_{cr}\mathbf{K}_G-8\mathbf{M}\theta_1^2\end{bmatrix}-\begin{bmatrix}\mathbf{M} & \mathbf{0} & \mathbf{0}\\ \mathbf{0} & \mathbf{0} & \mathbf{0}\\ \mathbf{0} & \mathbf{0} & \mathbf{0}\end{bmatrix}\theta_2^2=\mathbf{0}. \tag{21}$$

This procedure yields the second-order approximation of the first two instability with θ_2 being the second-order approximation of the parametric resonance frequency.

In all the above solution procedures, the parametric resonance frequency has to be double the value of the natural frequency of the loaded plate [12].

5. Numerical results

First, to validate this analysis, comparisons are made using a thick AISI 4340 steel plate ($L/h=12.5$) with both ends fixed. The critical buckling load and the first three natural frequencies are compared with those predicted by a NASTRAN 2D analysis performed using 10 CQUAD4 elements along the plate. The results are in very good agreement (Table 1).

Next, the numerical results are presented for the graphite/epoxy rectangular plates with symmetric cross-ply arrangements. The laminates are made out of eight

Table 1
Natural frequencies and buckling load for the AISI 4340 steel plate

	NASTRAN 2D	HOT
ω_1 [Hz]	331.45	336.35
ω_2 [Hz]	915.69	930.69
ω_3 [Hz]	1800.08	1840.36
P_{cr} [N]	572.83	569.70

identical plies with material properties: $E_1 = 1/344 \times 10^5$ MPa, $E_2 = E_3 = 1.034 \times 10^4$ MPa; $G_{12} = G_{13} = 4.999 \times 10^3$ MPa, $G_{23} = 1.999 \times 10^3$ MPa; $v_{12} = v_{13} = v_{23} = 0.33$. The plate has a length $L = 127$ mm and a width $b = 12.7$ mm. Two different plate thicknesses, $h = 1.016$ and 10.16 mm resulting in the two cases, $L/h = 125$ and $L/h = 12.5$, are analyzed. For both, isotropic and composite plates, the finite element analysis is performed using 10 quadrilateral elements with four nodes and eight degrees of freedom per node.

Two types of boundary conditions are studied: Case 1: wherein one of the short edges fixed and the opposite edge loaded with the dynamic buckling force and Case 2: wherein both short edges fixed and the dynamic buckling load applied on one of them, the long edges are free in both cases. The first natural frequency and the critical buckling load are computed for each combination of boundary conditions and thickness using CLPT, FSDT and HOT. The obtained results are compared with the experimental results of natural frequencies for the thin plate ($L/h = 125$) and Case-1 type boundary conditions [13]. For the thin plate ($L/h = 125$) in Case 1, a NASTRAN 3D analysis using ten CHEXA elements along the length of the plate and eight through the thickness, is also used for validation. These results, summarized in Table 2, indicate that the CLPT and the FSDT slightly overpredict the natural frequency, whereas the HOT results are closer to the experimental value and to the NASTRAN analysis. For both types of boundary conditions, the CLPT and FSDT overpredict the natural frequencies and the critical buckling load compared with the HOT. These deviations are more significant for thicker plates ($L/h = 12.5$). For example, using CLPT, the first natural frequency is overpredicted in Case 1 by 3.96 and in Case 2 by 20.04 percentages, whereas the FSDT overpredictions are 0.74 and 4.45 percentages in Cases 1 and 2, respectively. For the same thickness ratio ($L/h = 12.5$), the critical buckling load (P_{cr}) is overpredicted by the CLPT in Case 1 by 6.37 and in Case 2 by 71.91 percentages, whereas the FSDT overpredicts P_{cr} in Case 1 by 2.65 percent and in Case 2 by 8.84 percent. It is important to observe that the deviations increase with plate thickness. This is due to the fact that the transverse shear stresses, which increase with plate thickness, are modeled accurately using the HOT, whereas an adhoc shear correction factor is used in the FSDT and are completely ignored by the CLPT.

It must be noted that while the CLPT finite element model uses six degrees of freedom per model (equivalent to 24 per element), the FSDT and HOT based finite element models use eight degrees of freedom per node (equivalent to 32 per element). Thus, for the same mesh size, the computational efforts associated with FSDT and HOT are the same. However, the latter is more accurate even when the number of elements is half of that used in the FSDT (Table 3). Deviations between theories increase with plate thickness.

The variation of the first natural frequency (ω_1) of the plate loaded with $\alpha_0 P_{cr}$ is shown in Fig. 1 for Case 2 and $L/h = 12.5$. The results obtained from the present theory are compared with those obtained using the CLPT and FSDT. Once again, it is observed that the CLPT and FSDT overpredict the natural frequency.

The first-order approximation of the first two instability regions are presented for the thick composite plate in Fig. 2, where the parametric ratio ($\theta_1/2\omega_1$) is plotted with respect to the dynamic parameter α_1 for fixed values of the static parameter α_0. The parametric ratio is obtained by dividing the parametric resonance frequency (θ_1) resulting from Eqs. (18a)–(18c) by $2\omega_1$, the natural frequency of the loaded plate obtained by neglecting the harmonic term in Eq. (15). The quantity α_1 defines

Table 2
First natural frequency and buckling load for the composite plate

Case	L/h		CLPT	FSDT	Experimental [13]	NASTRAN 3D	HOT
1	125	ω_1 [Hz]	82.15	82.12	79.83	81.98	82.11
		P_{cr} [N]	16.43	16.38			16.33
2		ω_1 [Hz]	522.85	521.15			520.72
		P_{cr} [N]	261.62	260.11			259.73
1	12.5	ω_1 [Hz]	820.52	795.09			789.22
		P_{cr} [N]	16344	15772			15364
2		ω_1 [Hz]	4664.4	4058.6			3885.5
		P_{cr} [N]	261623	165644			152179

Table 3
The influence of mesh size on the first natural frequency of the composite plate

	Mesh size (Case 1) [elements/length × elements/width]					
	CLPT		FSDT		HOT	
	10×1	20×1	10×1	20×1	10×1	20×1
$L/h = 125$ ω_1 [Hz]	82.152	82.150	82.125	82.122	82.119	82.115
$L/h = 12.5$ ω_1 [Hz]	820.519	820.497	795.097	794.440	789.224	788.567

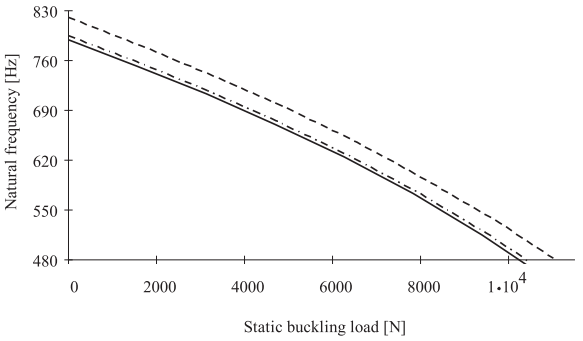

Fig. 1. The variation of the natural frequency of the plate with the static buckling load, Case 2, $L/h = 12.5$: (- - -) CLPT, (-·-·-·) FSDT, (—) HOT.

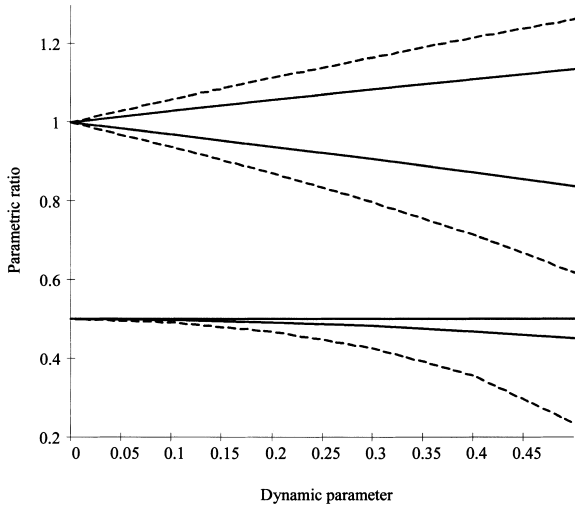

Fig. 2. The first-order approximation of the first two instability regions for the composite plate, Case 1, $L/h = 125$: (—) $\alpha_0 = 0.2$, (- - -) $\alpha_0 = 0.6$.

the amplitude of the dynamic component of the compressive force, whereas the static parameter α_0 defines the magnitude of static component of the compressive force (Eq. (14)). As seen from Fig. 2, the width of the instability regions increases with an increase in static and dynamic loads.

The four instability regions resulting from Eqs. (20a)–(20c) are shown in Fig. 3 for a static component of the buckling force of 60% of the critical buckling load. As only the first two instability regions have been observed experimentally [12], further results are presented only for these two regions.

The second approximation of the first two instability regions obtained by solving the Eq. (21) with the buckling force having a static component of 40% of the critical buckling load, is shown in Fig. 4. Comparisons are made with the results obtained using the first-order approximation of the first two instability regions for the thin composite plate in Case 2. For values of the dynamic parameter (α_1) greater than 0.2, the differences between the two approximations become more significant (Fig. 4).

To investigate the transverse shear effects, the results from the present theory are compared in terms of parametric resonance frequency with those obtained using the CLPT (Fig. 5) and FSDT (Fig. 6) for the thick composite plate in Case 2. Due to the presence of a significant transverse shear in thick composites, maximum deviations are observed from the CLPT, which completely ignore the shear effects. Noticeable devia-

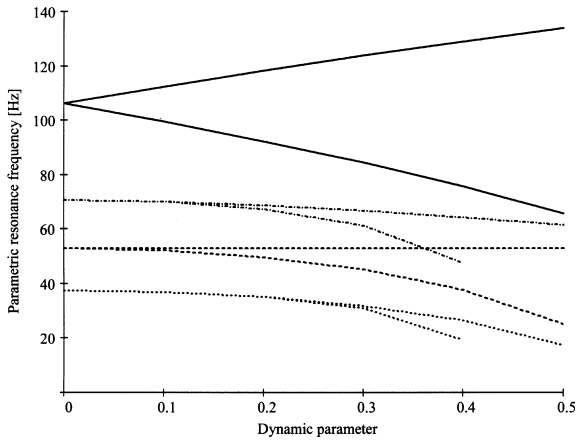

Fig. 3. Four instability regions of the composite plate, Case 1, $L/h = 125$, $\alpha_0 = 0.6$: (—) First instability region, (- - -) second instability region, (-·-·-·) third instability region, (···) fourth instability region.

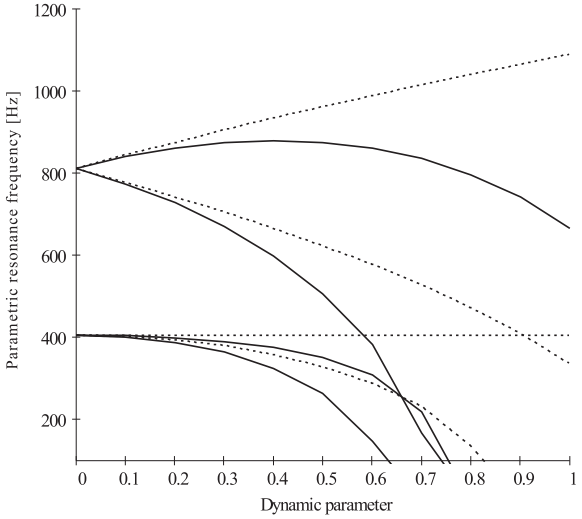

Fig. 4. First- and second-order approximations of the instability regions for the composite plate, Case 2, $L/h = 125$, $\alpha_0 = 0.4$: (- - -) First order approximation, (—) second order approximation.

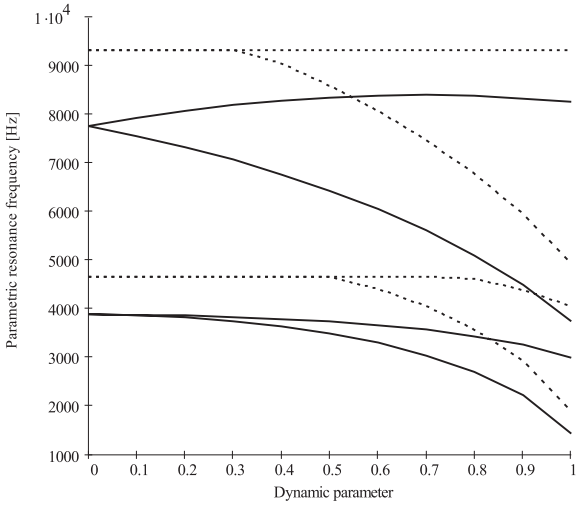

Fig. 5. Comparison between the second-order approximation of the instability regions of the composite plate using the CLPT and HOT, Case 2, $L/h = 12.5$, $\alpha_0 = 0$: (—) HOT, (- - -) FSDT.

tions in the instability regions are observed from the FSDT.

6. Concluding remarks

A higher order plate theory based finite element model has been developed for studying the parametric instability of composite plates. The theory assumes through the thickness cubic variations for in-plane displacements and satisfies the stress free boundary conditions. The numerical results are presented for both isotropic and $[(0/90)_2]_s$ graphite/epoxy composite plate with two different boundary conditions and plate thicknesses. The following observations are made from this study:

1. The natural frequencies and the critical buckling loads determined from the current approach for isotropic plates are in good agreement with those obtained from the NASTRAN 2D analysis. For composite plates, excellent correlation is observed in natural frequency with available experimental data and results obtained using the NASTRAN 3D analysis.
2. Both the classical and the first-order theories overpredict the natural frequencies and the critical buckling load for both types of boundary conditions studied. The deviations increase with plate thickness due to increased transverse shear effects.
3. The width of the instability regions increases with an increase in both, static and dynamic loads, as expected. The instability regions are also affected by the transverse shear effects. Deviations increase with plate thickness.
4. The differences between the first- and second-order approximations of the instability regions increase with the increase in the dynamic load.

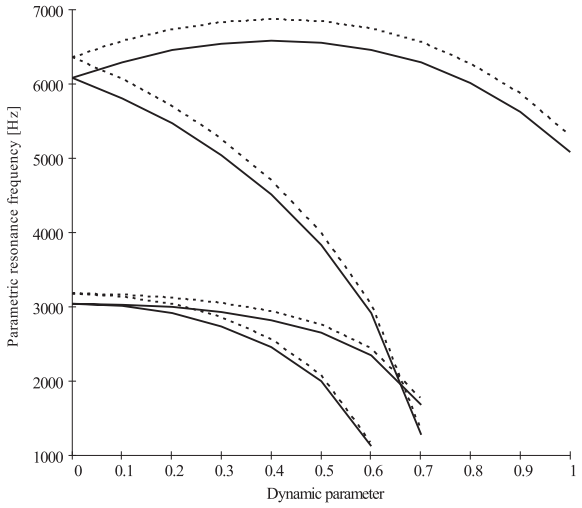

Fig. 6. Comparison between the second-order approximation of the instability regions of the composite plate using the FSDT and HOT, Case 2, $L/h = 12.5$, $\alpha_0 = 0.4$: (—) HOT, (- - -) FSDT.

Acknowledgements

The support of the present research by the US Army Research Office, Grant # DAAH04-94-G-0157, Technical Monitor, Dr. Gary Anderson is acknowledged.

The authors are also thankful to Dr. Haozhong Gu and to Dan Dragomir-Daescu, the Arizona State University, for their valuable comments during the research.

References

[1] Bert CW. Dynamic instability of shear deformable antisymmetric angle-ply laminates. Int J Solids Struct 1987;23:1053–61.
[2] Srinivasan RS, Chelepandi P. Dynamic stability of rectangular laminated composite plates. Comp Struct 1986; 24:233–8.
[3] Balamurugan M, Ganapathi M, Varadan TK. Nonlinear dynamic instability of laminated composite plates using finite element method. Comp Struct 1996;60: 125–30.
[4] Reddy JN, Phan ND. Stability and vibration of isotropic, orthotropic and laminated plates according to a higher-order shear deformation theory. J Sound and Vibr 1985;98:157–70.
[5] Librescu L, Khdeir AA. Analysis of symmetric cross-ply laminated elastic plates using a higher-order theory: part II – buckling and free vibration. Composite Struct 1988; 9:259–77.
[6] Chattopadhyay A, Gu H. Exact elasticity solution for buckling of composite laminates. Composite Struct 1996; 34:291–9.
[7] Reddy JN. A simple higher-order theory for laminated composite plates. J Appl Mech 1984;51:745–52.
[8] Reddy JN. Mechanics of laminated composite plates. Boca Raton, FL: CRC Press, 1997.
[9] Timoshenko SP, Gere JM. Theory of elastic stability. New York: McGraw-Hill, 1961.
[10] Pica A, Wood RD, Hinton E. Finite element analysis of geometrically nonlinear plate behavior using a Mindlin formulation. Comp Struct 1980;11:203–15.
[11] Zienkiewicz OC, Taylor RL. The finite element method. New York: McGraw-Hill, 1991.
[12] Bolotin VV. The dynamic stability of elastic systems. San Francisco, CA: Holden-Day, 1964.
[13] Shen MHH, Grady JE. Free vibrations of delaminated beams. AIAA Journal 1992;60:1361–70.